Sleeve Design of Permanent-magnet Machine for Low Rotor Losses*

Junqiang Zheng[1*], *Wenxiang Zhao*[1], *Jinghua Ji*[1], *Jihong Zhu*[2] *and Christopher H. T. Lee*[3]
(1. School of Electrical and Information Engineering, Jiangsu University, Zhenjiang 212013, China;
2. Department of Computer Science and Technology, Tsinghua University, Beijing 100000, China;
3. School of Electrical and Electronic Engineering, Nanyang Technological University, 639798, Singapore)

Abstract: In this study, a novel rotor sleeve for permanent-magnet (PM) machines equipped with fractional-slot concentrated-windings (FSCW) is proposed. With the newly designed rotor sleeve, the rotor eddy-current (EC) losses are significantly reduced, and the torque density of the machine is improved. First, the rotor EC losses of a surface-mounted PM machine with the sleeve are analyzed. Meanwhile, the sleeve EC barriers and PM segmentation technologies for the suppression of the rotor EC losses are evaluated. Subsequently, an FSCW PM machine with the newly designed sleeve is proposed and optimized for a given set of specifications. Its electromagnetic and mechanical performances are evaluated by the finite element method (FEM). Finally, three assembling methods are presented and assessed comprehensively in terms of their merits and drawbacks.

Keywords: Permanent-magnet machine, rotor losses, sleeve, eddy-current, concentrated-windings

1 Introduction

Permanent-magnet (PM) machines have recently become more attractive in electric vehicle applications, owing to their compacted structure, high torque/power density, and high efficiency [1-4]. PM machines equipped with fractional-slot concentrated-windings (FSCW) are preferable to achieve high fault-tolerance capability and improved efficiency [4-6]. The FSCW PM machines offer a high slot fill factor, short non-overlapping end windings, low cogging torque, sinusoidal back-electromotive force (EMF), high fault-tolerance capability, and excellent magnetic isolation as well as thermal insulation. However, one of the key challenges of utilizing FSCW is their high rotor losses, especially in the rotor sleeve, at high-speed operations. The high rotor losses are mainly caused by the abundant stator magneto-motive force (MMF) harmonics. The gathering of excessive rotor losses inside PM machines generate excessive heat. This may cause the irreversible demagnetization of the PM and other adverse effects [7-10].

The rotor eddy-current(EC) losses can be suppressed by three major aspects, namely, cancelling the MMF harmonics, weakening the armature reaction magnetic field, and limiting the EC paths. In Refs. [11-12], a multi-layer windings configuration was adopted to reduce the stator MMF harmonics. The star-delta hybrid connection windings configuration was systematically studied in Ref. [13] to reduce the MMF sub-harmonics by shifting the current phase angle. Additionally, multi-phase and phase-shift designs were adopted in Refs. [14-15] to reduce EC losses. However, these methods relatively changed the FSCW configuration, and may deteriorate the inherent fault-tolerant capability of concentrated-windings. In Refs. [16-17], appropriate flux barriers were arranged in a rotor yoke to reduce EC losses. An analytical expression was simultaneously derived by the simplified permeance model. Some literatures have reported the reduction of rotor losses by limiting the EC flowing paths. In Ref. [18], the circumferential and axial grooves were studied to reduce EC losses. The influences of the sleeve thickness on the rotor EC losses and various composition structures of carbon fiber and stainless steel were presented in Ref. [19].

Manuscript received May 27, 2020; revised August 3, 2020; accepted August 19, 2020. Date of publication December 31, 2020; date of current version December 10, 2020.
* Corresponding Author, E-mail: 2289832202@qq.com
* Supported by the National Natural Science Foundation of China (51991383), the Natural Science Foundation of Jiangsu Province (BK20171298), the Graduate Scientific Research Innovation Project of Jiangsu Province (KYCX18_2248) and the Priority Academic Program Development of Jiangsu Higher Education Institutions.
Digital Object Identifier: 10.23919/CJEE.2020.000033

Generally, PM segmentation is a plain and valid method for reducing rotor EC losses. Moreover, it has a slight effect on the electromagnetic performances of electric machines [20-21]. However, because of the requirement of high mechanical strength, sleeve EC losses cannot be reduced by the PM segmentation technique. The sleeve EC losses increase significantly with the increment of the speed and electrical load. Moreover, it is very difficult to improve the magnetic load of PM machines equipped with a rotor sleeve, therefore, achieving high torque density and high efficiency becomes challenging.

In this study, a novel sleeve structure is proposed to significantly reduce the rotor losses and improve the torque density of FSCW PM machines. The related loss-reducing techniques are evaluated in detail. In Section 2, the distribution of the rotor losses, equivalent resistance model, rotor sleeve EC barriers and rotor PM segmentation are presented. In Section 3, a PM machine equipped with the novel sleeve is designed and its topology and characteristics are analyzed. The finite-element method (FEM) is used to assess its performance, including the back electromotive forces (EMFs), torque and its ripple, rotor EC losses, and mechanical strength, and presented in Section 4. Finally, three assembly methods are presented in Section 5.

2 Analysis of rotor losses

2.1 Rotor losses of PM machine with sleeve

It is well-known that significant rotor losses are normally generated inside PM machines, especially at high speed operations [22-23]. Fig. 1 shows a traditional surface-mounted PM machine with a sleeve. Its main parameters are listed in Tab. 1. The rotor losses, which mainly include the sleeve and PM EC losses, have a significant influence on the performance of PM machines. The high rotor losses and poor heat dissipation ability may cause disadvantageous effects such as extremely high temperatures, irreversible demagnetization, structural deformation, and insulation failure. Therefore, it is essential to reduce the rotor losses of PM machines. Both sleeve EC losses and PM EC losses are closely related to the rotor speed. Fig. 2 shows the relationship between the EC losses and speed of the PM machines under the i_d=0 control strategy. It should be noted that n_0 is the rated speed, and the sleeve EC losses at the speed of n_0 are assumed to be 1. It can be observed that the sleeve EC losses play a dominating role, accounting for approximately 75%. Accordingly, this study focuses on reducing the sleeve EC losses of the PM machine.

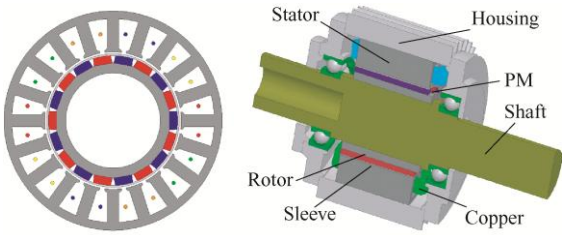

Fig. 1 Traditional surface-mounted PM machine with sleeve

Tab. 1 Main parameters of the surface-mounted PM machine

Item and symbol	Surface-mounted PM machine
Outer diameter of stator/mm	120
Inner diameter of stator/mm	75
Outer diameter of PM R_{pm}/mm	36
Axial length/mm	60
Air-gap length/mm	0.5
Sleeve length L_{sl}/mm	1
Thickness of PM/mm	4.4
Polar arc coefficient	0.92
PM tilt angle α/(°)	18
Turns per phase	30
Rated current/A	16
Rated speed/(r/min)	6 000
PM material	NdFe40H
Remanence of PM/T	1.28
Sleeve material	Stainless steel 304
Conductivity of sleeve/(S/m)	1 390 000
Iron core lamination	B20AT1500

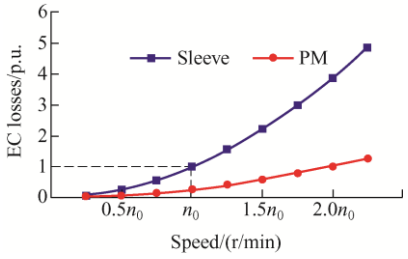

Fig. 2 Relationship of EC losses with speed of PM machine with sleeve

2.2 Equivalent analysis model of EC losses

Presently, the most common methods for reducing sleeve and PM EC losses are sleeve barriers and PM segmentation [24-25]. Fig. 3 presents the equivalent resistance of sleeve EC barriers and PM segmentation, as well as the original for comparison. It

can be observed that both the EC barriers and PM segmentation can change the paths of the EC. The resistance on the EC paths can be defined as

$$R = r_0 \oint_l f(l)\mathrm{d}l \tag{1}$$

where r_0 is the resistance of a unit length of EC paths and $f(l)$ is a function of the EC paths. It can then be simplified as

$$f(l)=\begin{cases} 2(L_{\mathrm{ef}}+L_{\mathrm{r}}) & \text{Original model} \\ f(x,N_{\mathrm{b}}) & \text{EC barriers} \\ 2(S_{\mathrm{cir}}L_{\mathrm{ef}}+S_{\mathrm{shaft}}L_{\mathrm{r}}) & \text{Segmentations} \end{cases} \tag{2}$$

where L_{ef} and L_{r} are the equivalent lengths of the rotor PMs in the axial and circumferential directions, respectively. Further, $f(x, N_{\mathrm{b}})$ is an abstract function that is closely related to the shape, size, and number of EC barriers. S_{cir} and S_{shaft} are the PM segmentation numbers in the axial and circumferential directions, respectively. It is necessary to explain the following two points as follows.

(1) For the EC barriers model, the EC paths are changed in different equivalent resistance models. Moreover, the functions of the EC paths cannot be expressed by specific formulas. This is because the shape, size, and position of the EC barriers have a significant influence on these functions.

(2) In the segmentation model, the EC paths are limited in small PM blocks. In this case, the function of the EC paths can be expressed quantitatively in terms of the number of circumferential and axial segmentations.

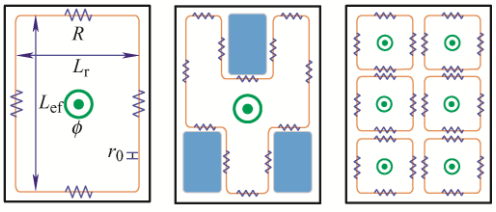

(a) Original mode1 (b) EC barriers (c) Segmentations

Fig. 3 Schematic of equivalent resistance

2.3 Sleeve EC barriers

The sleeve EC barriers technique has the potential to increase the equivalent resistance and hence reduce EC losses. The losses-reduction effect varies with the number and location of the rotor sleeve EC barriers. Fig. 4 illustrates three types of sleeves, which include an original one and two other types with different EC barriers. Type I has eight EC barriers evenly distributed in the sleeve circumference. In type II, the number of EC barriers is doubled and they are distributed as a specific rule. These rotor sleeves are fabricated by stainless steel 304 with a conductivity of 1 390 000 S/m.

The sleeve EC losses and maximum equivalent stress for the different sleeve structures are shown in Fig. 5. It is worth noting that the maximum equivalent stress is calculated at a speed of 10 000 r/min (approximately 1.7 times rated speed). As can be observed, the sleeve EC losses of type II are smaller than those of type I and the original one. Compared to the original one, the EC losses of type II are reduced by approximately 84%. Because of the increased barriers and asymmetric distribution, there are fewer EC losses in type II than in type I. Particularly, the number and location of the sleeve EC barriers have a significant influence on the sleeve EC losses. The maximum equivalent stress increases with the number of barriers. Considering the tensile strength of the sleeve material, i.e., approximately 215 MPa, it can be stated that the rotor with the sleeve structure can be safely operated for a long time.

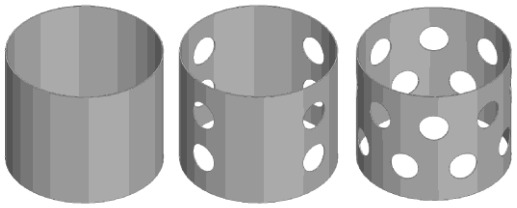

(a) Original (b) Type Ⅰ (c) Type Ⅱ

Fig. 4 Types of rotor sleeves

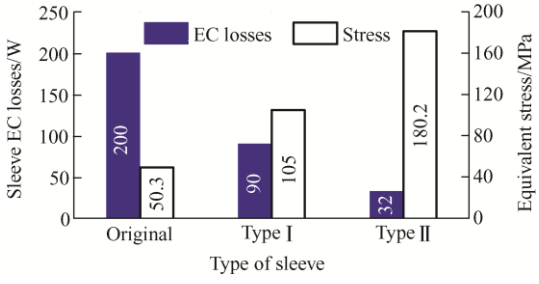

Fig. 5 EC losses and maximum equivalent stress

The 3D EC distributions of the rotor sleeve with EC barriers, are presented in Fig. 6. The EC loops are represented by the black solid line with arrows. It can be observed that the EC density is significantly reduced by adopting the sleeve EC barriers. This is because they lengthen the EC paths significantly,

reducing the EC density. Additionally, because the FSCW PM machines suffer abundant MMF harmonics, which induce different EC loops, the distribution of the sleeve EC is very complicated and irregular. Some of the large EC loops are mixed with several small EC loops because the EC flows in the direction of less resistance.

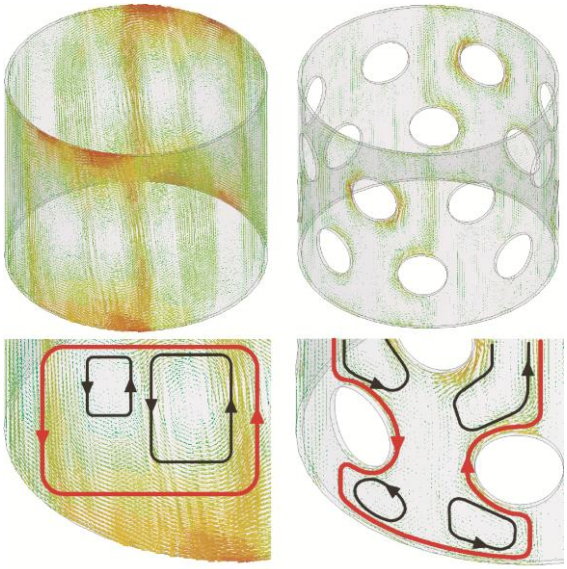

(a) Original (b) With EC barriers

Fig. 6 3D EC distributions of rotor sleeve

2.4 PM segmentation

Generally, suppressing the EC losses by PM segmentation is affected by the stator space and current pulse width modulation harmonics. Both of them complicate the distribution of EC in PMs. To clearly explain the underlying relationship between segmentations, i.e., harmonic and EC, only the stator space harmonic is considered in this study. Nowadays, a significant number of literatures has reported the adoption of PM segmentation to reduce PM EC losses [26-27]. Fig. 7 shows the 3D EC density distribution of the rotor PMs. It should be noted that they are within the same color scale, representing values of 0 to 4.0×10^6 A/m^2. It can be observed that the EC is confined within a piecewise PM block. Additionally, the EC distributions of each PM segment are regular. In other words, the EC loops are distributed uniformly within the small PM blocks. However, they are different from the EC distributions of the sleeve as previously shown in Fig. 6.

To better understand the effect of PM circumferential and axial segmentations on EC losses, the PM EC losses of the PM machine are presented in Fig. 8. Mark 1 and 2 represent the number of circumferential and axial segmentations, respectively. It can be observed that both the axial and circumferential PM segmentations can effectively reduce the EC losses. The rotor PM EC losses are significantly reduced as the number of PM segmentations increase. However, the EC losses are no longer reduced when the number of segmentations increases to certain values referred to as the "saturation state". Moreover, the reduction of EC losses by the circumferential segmentations is more obvious than that of the axial counterpart. This is because the rotor PMs are divided into $2p$ (p is pole pairs of PM) segments. For example, an 18-pole PM machine divides its PM into 18 segments.

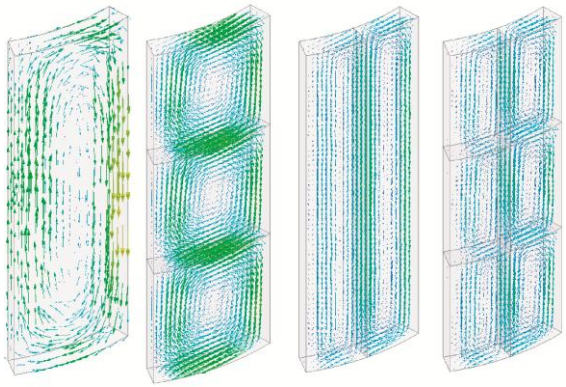

(a) Original (b) Three (c) Two (d) Six

Fig. 7 EC distributions of rotor PMs with different segments

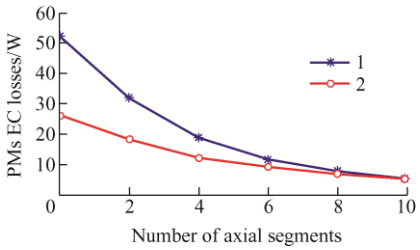

Fig. 8 PM EC losses of PM machine

3 Structure and characteristics of new sleeve

3.1 Structure

The proposed 5-phase 20s18p PM machine with the novel designed sleeve is presented in Fig. 9. The fault-tolerant teeth (FTT) and FSCW configuration are adopted into the PM machine to improve its fault-tolerance capability. It should also be noted that

the PM machine interphases can be magnetically decoupled. Fig. 10 illustrates the FSCW configuration of the present PM machine. The mechanical angle α_m of adjacent slots is expressed as

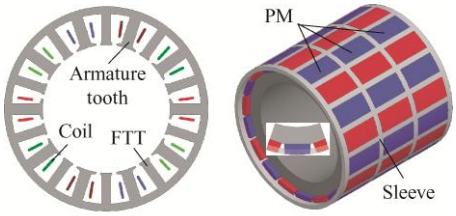

(a) Stator (b) Rotor

Fig. 9 Proposed 20s18p PM machine

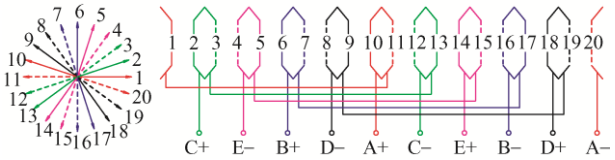

Fig. 10 20s18p windings configuration

$$\alpha_m = \frac{360^\circ}{N_s} \tag{3}$$

where N_s is the number of slots. According to Eq. (3), the value of α_m in the PM machine is 18°. Because the pitch between coils A+ and A− is 10, the angle-difference between them is 180°. Moreover, their wound direction is opposite. Therefore, the actual angle-difference between coils A+ and A− becomes 0°. Consequently, the phase back-EMFs in the PM machine double the coil EMFs. The main design parameters of the proposed machine are listed in Tab. 2.

Tab. 2 Main design parameters of the proposed machine

Item and symbol	Proposed machine
Outer diameter of stator/mm	120
Inner diameter of stator/mm	75
Outer diameter of PM R_{pm}/mm	37
Axial length/mm	60
Air-gap length/mm	0.5
Sleeve length L_{sl}/mm	2
Thickness of PM/mm	4.4
Polar arc coefficient	0.92
PM tilt angle α/(°)	18
Turns per phases	30
Rated current/A	16
Rated speed/(r/min)	6 000
PM material	NdFe40H
Remanence of PM/T	1.28
Sleeve material	Stainless steel 304
Conductivity of sleeve/(S/m)	1 390 000
Iron core lamination	B20AT1500

The novel rotor sleeve is designed in a frame structure that can be matched with the rotor PMs. To improve the clarity of description, a 2D section schematic is illustrated in Fig. 11, and compared with the conventional one. In Fig. 11, "a" represents the tilt angle of the PMs. It can be observed that the newly designed sleeve structure reduces the thickness of the equivalent air-gap length. To precisely and firmly fix the PMs, the sleeve of each pole is fitted with a suitable angle and trapezoidal shape. Because the PM is divided into many segments and embedded in the matched frame sleeve, the shear stress at the edge of a single PM is weakened, avoiding the risk of cracking for the PM.

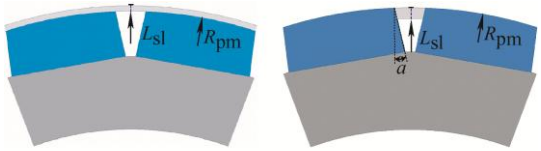

(a) Original (b) Newly designed

Fig. 11 2D section schematics

3.2 Characteristics

The newly designed sleeve structure is characterized by a reduced equivalent air-gap thickness, which improves the torque density. Particularly, the output torque of the PM machine equipped with the newly designed rotor sleeve can be increased without changing the electric load. Because the frame sleeve structure is equivalent to the EC barrier on the surface of the rotor sleeve, as previously presented in Section 2.3, the sleeve EC losses can be significantly reduced. However, the rotor PMs should also be divided into small segments because the PMs are matched with the newly designed rotor sleeve. The correspondence is presented in Section 2.4.

The PM machine equipped with the newly designed rotor sleeve not only offers high torque density but also less sleeve EC and PM EC losses. However, there are some challenges. First, the strength of the newly designed sleeve is a matter of concern. The shear stress on the edges of the PMs damages them. In Section 4.4, the ANSYS Workbench 18.2 is used to evaluate the mechanical performances of the new design. Second, matching the newly designed sleeve and PM segments is challenging. Assembling the PMs and sleeve requires extremely accurate

processing techniques. Third, installing the rotor structure is a challenging process. Section 5 presents related descriptions of the PM installation with the new rotor sleeve structure.

4 Performance evaluation

In this Section, the performance of the 20s18p PM machine equipped with the newly designed sleeve is evaluated in comparison with the conventional one. For a fair comparison, their sides are optimally designed with similar dimensions, slot filling factors, materials, electric load, and working conditions.

4.1 Back-EMFs

The FEM-predicted no-load back-EMFs, and the spectrums of the two machines at the same rotational speed of 6 000 r/min are exhibited in Fig. 12. It can be observed clearly that both the original and newly designed PM machines have flat-topped back-EMF waveforms. However, the newly designed PM machine exhibits higher no-load back-EMFs than the original one. From Fig. 12b, it can be observed that the amplitude of the fundamental harmonic component of the newly designed PM machine is higher than that of the original one, which is improved by approximately 15%. Moreover, both PM machines have the highest 3rd order harmonic, which causes the flat-topped back-EMF waveforms.

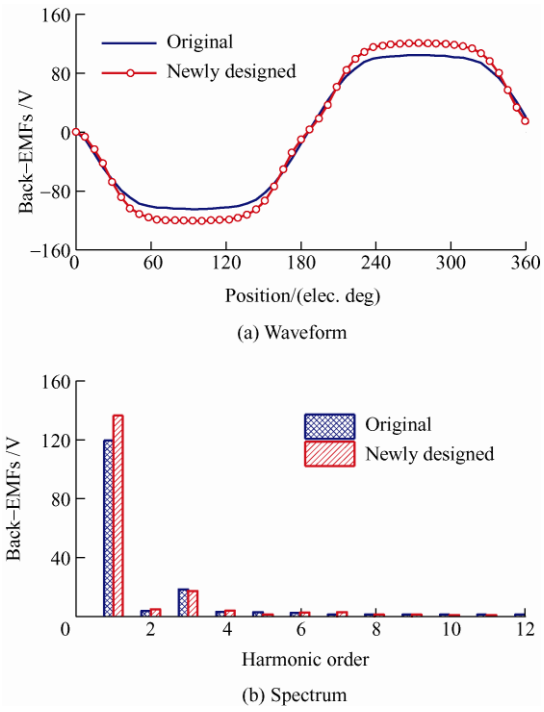

Fig. 12 Back-EMFs of both PM machines

4.2 Electromagnetic torque

Because the average torque of surface-mounted PM machines only consists of the PM torque component, their electromagnetic torque can be expressed as

$$T_e = \frac{m}{2} p \psi_f i_s \tag{4}$$

where ψ_f is the PM flux linkage and i_s is the current. Their torque profiles are presented in Fig. 13. Because of the reduced equivalent air-gap length, the newly designed PM machine attains a higher average torque than that of the conventional one. Additionally, both FSCW PM machines exhibit very little torque pulsation because of their small cogging torques.

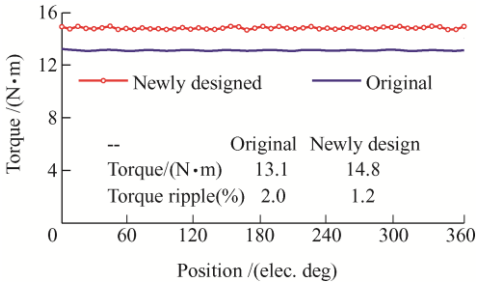

Fig. 13 Electromagnetic torque

4.3 Rotor EC losses

The heat dissipation of the rotor is very significant, in comparison to other heating components [28-29]. Therefore, it is highly essential to reduce the rotor losses of the PM machines. The electromagnetic losses of both machines are calculated using FEM under a rated operating condition, i.e., n=6 000 r/min and I=16 A. Their corresponding losses are presented in Fig. 14. It can be observed that the sleeve EC losses of the newly designed machine are significantly reduced by approximately 94%. The PM EC losses are also decreased by approximately 35%. However, the iron losses of the newly designed PM machine are slightly higher than those of the original one. Among these losses, the sleeve EC losses are the dominating components in the original PM machine, and can be suppressed by the newly designed sleeve structure.

The electromagnetic losses of the original and newly designed PM machines at different speeds and currents are calculated and presented in Figs. 15 and 16, respectively.

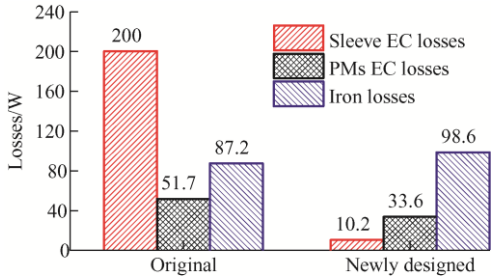

Fig. 14 Losses of both PM machines

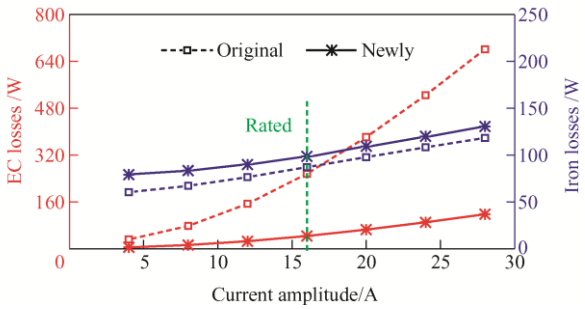

Fig. 15 Variation of losses by current amplitude of both PM machines (n=6 000 r/min)

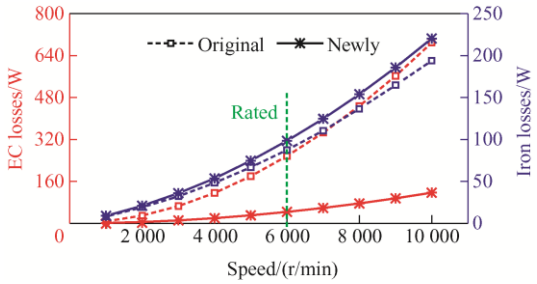

Fig. 16 Variation of losses by speed of both machines (I=16 A)

The following deductions can be made.

(1) The EC losses vary significantly with the current and speed variations. The PM machine with the newly designed sleeve, significantly reduces the rotor EC losses.

(2) The iron losses change slightly with the current variation, but change significantly with the speed variation. This is because the armature reaction magnetic field has little effect on the flux density of the stator iron core, whereas the alternating frequency of the magnetic field has a significant effect on the iron losses. Because of the enhancement of the PM magnetic field, the iron losses of the newly designed PM machine are slightly higher than those of the original one.

(3) When the current and speed are increased, the reduction of EC losses in the newly designed structure is more obvious. Particularly, the new sleeve structure is more suitable for high-torque and high-speed PM machines.

(4) The relationship between the iron core and EC losses with the current and speed variations can be used as an important criterion for indirect loss separation.

4.4 Mechanical strength of rotor sleeve

As mentioned above, the newly designed PM machine requires mechanical strength. It is necessary to predict the mechanical stress distribution of the new rotor sleeve. In this section, the ANSYS Workbench 18.2 is used to evaluate the equivalent (Von-Mises) stress. Fig. 17 shows the equivalent stress of the novel

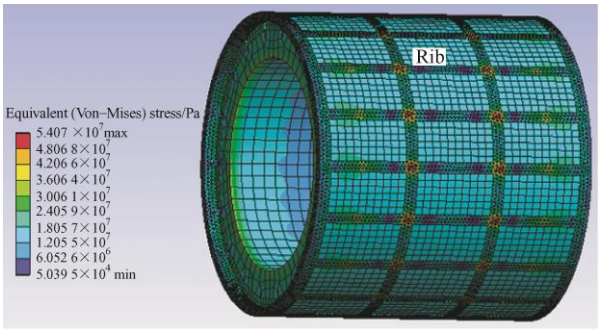

(a) Mesh and entire rotor

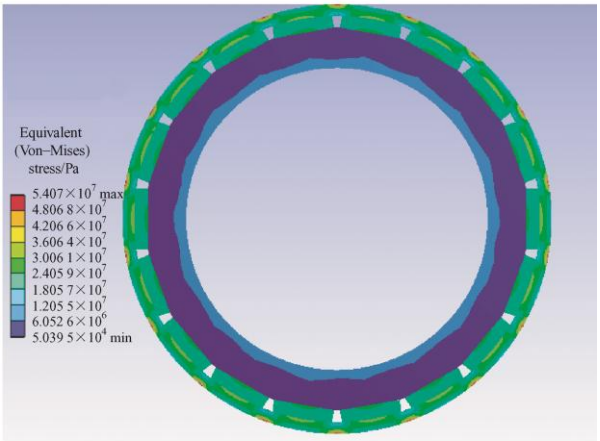

(b) Circumferential

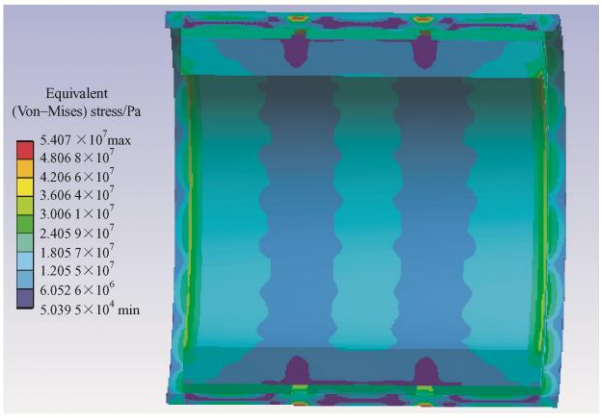

(c) Axial

Fig. 17 Equivalent stress of novel sleeve structure

sleeve structure at a speed of 10 000 r/min, and radial electromagnetic force F_e=20 MPa (direction: radial outward) for a single PM. Particularly, the electromagnetic force is calculated by the Fields Calculator of Maxwell 2D. It should be noted that the "Rib" is marked in Fig. 17. When the Rib number is increased, the mechanical stress distribution becomes more uniform. This effectively prevents large shear stress on the edges of the PMs. From Fig. 17a, it can be observed that the maximum stress position is the crossing area of the sleeve. It is approximately 54 MPa lower than the yield of the sleeve material. From Figs. 17b and 17c, there is no significant shear stress at the contacting edge of the PMs and sleeve.

To understand the relationship between the Ribs number and equivalent stress, the variations between the maximum equivalent stress and Ribs number are shown in Fig. 18, in comparison with the conventional sleeve marked with a dotted line. As the number of Ribs increases, the maximum equivalent stress is reduced. The maximum equivalent stress is approximately equal to that of the conventional one when the Rib number is large. When the number of Ribs is 3, the stress is greatly reduced and this becomes the optimal Ribs number. The maximum equivalent stress is calculated at 1.7 times the rated speed and still meets the requirements.

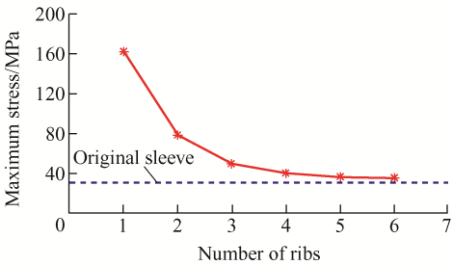

Fig. 18 Maximum equivalent stress variation by the number of ribs of newly designed PM machine

5 Installation of rotor PMs and sleeve

One of the key challenges of the newly designed PM machine is the assembling of the rotor sleeve and rotor part. In this section, three feasible methods are presented, namely, interference assembling of the rotor core, interference assembling of the rotor sleeve, and welding assembling of the entire rotor.

5.1 Interference assembling of rotor core

The schematic of the interference assembling of the newly designed PM machine rotor core is shown in Fig. 19, where the simple installation order is marked. First, it is necessary to insert isolated PM pieces into the corresponding slot of the rotor sleeve. It should be noted that precise dimension machining and assembling technology is required in this process. Subsequently, the rotor core is treated at a low temperature to achieve the effects of thermal expansion and cold contraction. It should be noted that this process requires high-quality thermal treatment technology. Finally, the rotor core is installed onto the inner surface of the PMs and pasted using high-performance glue. Skilled precise interference and clearance assembling technology is required during this process. To avoid PM extrusion, the size of the sleeve notch should be slightly smaller than that of the PMs.

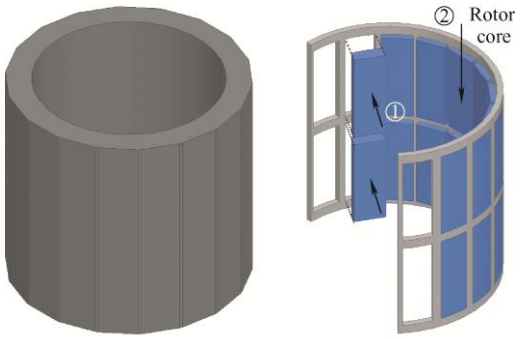

Fig. 19 Schematic of interference assembly of rotor core

5.2 Interference assembling of rotor sleeve

Fig. 20 illustrates the schematic of the interference assembling of the rotor sleeve. It should be noted that this process is different from the assembling process presented in Section 5.1, which requires high-temperature heat treatment of the rotor sleeve. At the beginning of this process, the isolated rotor PM pieces are pasted to the surface of the rotor core using high-performance glue. The heat-treated sleeve is then installed onto the rotor core. Similarly, skilled precise interference and clearance assembling technology is required during this process. The size of the rotor sleeve notch is also slightly smaller than that of the PMs to avoid extruding them.

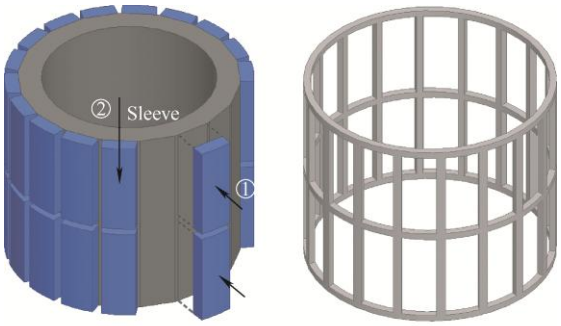

(a) Rotor iron core and PMs (b) Rotor sleeve

Fig. 20 Schematic of interference assembly of rotor sleeve

5.3 Welding assembling

The third assembling method is welding. The schematic of the welding assembling is presented in Fig. 21 where the process order and solder joints are marked. Moreover, the solder joint section is trapezoidal as shown in the frame. Similar to the second method, the isolated PM pieces are pasted to the surface of the rotor core using high-performance glue. Discrete stainless steel bars are then welded to the steel rings. Finally, grind treatment is needed for the welding points. Although the welding process is more complicated, this assembling method is the easiest and most convenient, compared to the other assembling methods.

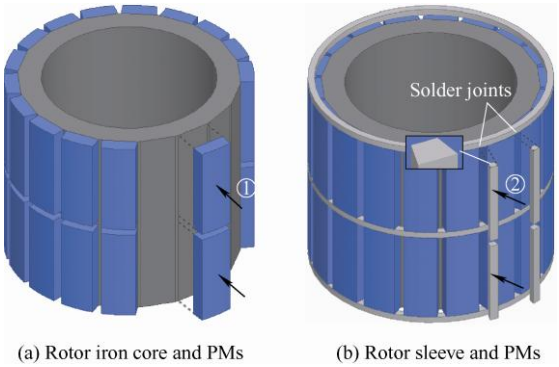

(a) Rotor iron core and PMs (b) Rotor sleeve and PMs

Fig. 21 Schematic of welding assembly

6 Conclusions

In this study, the rotor EC losses of PM machines were evaluated in detail. The EC barriers and PM segmentations were comprehensively analyzed as well. The results indicated that rotor EC losses can be effectively reduced using EC barriers and PM segmentation techniques. The loss-reduction is closely related to the distribution and number of EC barriers, as well as the number and direction of PM segmentation. A five-phase 20s18p PM machine equipped with the newly designed sleeve, was proposed and its electromagnetic performances evaluated and compared. The newly designed PM machine achieved lower rotor losses and a higher torque density under the same electric load without basically affecting the mechanical properties. Finally, three assembling methods, namely, interference assembling of the rotor core, interference assembling of the rotor sleeve, and welding assembling, were studied and employed for the installation of the entire rotor.

References

[1] Q Chen, Y Yan, G Liu, et al. Design of a new fault-tolerant permanent magnet machine with optimized salient ratio and reluctance torque ratio. *IEEE Trans. Ind. Electron*., 2020, 67(7): 6043-6054.

[2] P Ramesh, N C Lenin. High power density electrical machines for electric vehicles-comprehensive review based on material technology. *IEEE Trans. Magn*., 2019, 55(11): 0900121.

[3] S J Rind, Y Ren, Y Hu, et al. Configurations and control of traction motors for electric vehicles: A review. *Chinese Journal of Electrical Engineering*, 2017, 3(3): 1-17.

[4] A EL-Refaie. Fractional-slot concentrated windings synchronous permanent-magnet machines: Opportunities and challenges. *IEEE Trans. Ind. Electron*., 2010, 57(1): 107-121.

[5] A M El-Refaie, T M Jahns, D W Novotny. Analysis of surface permanent magnet machines with fractional-slot concentrated windings. *IEEE Trans. Energy Convers*., 2006, 21(1): 34-43.

[6] S U Chung, J W Kim, Y D Chun, et al. Fractional-slot concentrated-winding PMSM with consequent pole rotor for a low-speed direct drive: Reduction of rare earth permanent magnet. *IEEE Trans. Energy Convers*., 2015, 30(1): 103-109.

[7] S S Nair, V I Patel, J Wang. Post-demagnetization performance assessment for interior permanent magnet AC machines. *IEEE Trans. Magn*., 2016, 52(4): 8102810.

[8] G Du, W Xu, J Zhu, et al. Power loss and thermal analysis for high-power high-speed permanent magnet machines. *IEEE Trans. Ind. Electron*., 2020, 67(4): 2722-2733.

[9] G Choi, Y Zhang, T M Jahns. Experimental verification of rotor demagnetization in a fractional-slot concentrated-winding PM synchronous machine under drive fault conditions. *IEEE Trans. Ind. Appl*., 2017, 53(4): 3467-3475.

[10] T Hosoi, H Watanabe, K Shima. Demagnetization analysis of additional permanent magnets in salient-pole synchronous machines with damper bars under sudden short circuits. *IEEE Trans. Ind. Electron*., 2012, 59(6): 2248-2456.

[11] X Chen, J Wang. Magnet-motive force harmonic reduction techniques for fractional-slot non-overlapping winding configurations in permanent-magnet synchronous machines. *Chinese Journal of Electrical Engineering*, 2017, 3(2): 102-113.

[12] A S Abdel-Khalik, S Ahmed, A M Massoud. Effect of multilayer windings with different stator winding connections on interior PM machines for EV applications. *IEEE Trans. Magn*., 2016, 52(2): 8100807.

[13] W Zhao, J Zheng, J Ji, et al. Star and delta hybrid connection of fractional-slot concentrated-windings PM machine for low space harmonics. *IEEE Trans. Ind. Electron*., 2018, 65(12): 9266-9279.

[14] X Chen, J Wang, V I Patel, et al. A nine-phase 18-slot 14-pole interior permanent magnet machine with low space harmonics for electric vehicle applications. *IEEE Trans. Energy Convers*., 2016, 31(3): 860-871.

[15] A S Abdel-Khalik, S Ahmed, A M Massoud. Low space harmonics cancelation in double-layer fractional slot winding using dual multiphase winding. *IEEE Trans. Magn*., 2015, 51(5): 8104710.

[16] J Zheng, W Zhao, J Ji, et al. Design to reduce rotor loss in fault-tolerant permanent-magnet machines. *IEEE Trans. Ind. Electron*., 2018, 65(11): 8476-8487.

[17] L Alberti, E Fornasiero, N Bianchi. Impact of the rotor yoke geometry on rotor losses in permanent-magnet machines. *IEEE Trans. Ind. Appl*., 2012, 48(1): 98-105.

[18] J Shen, H Hao, M Jin, et al. Reduction of rotor eddy current loss in high speed PM brushless machines by grooving retaining sleeve. *IEEE Trans. Magn*., 2013, 49(7): 3973-3976.

[19] L Li, W Li, D Li, et al. Influence of sleeve thickness and various structures on eddy current losses of rotor parts and temperature field in surface mounted permanent-magnet synchronous motor. *IET Electr. Power Appl*., 2018, 12(8): 1183-1191.

[20] X Wu, R Wrobel, P H Mellor, et al. A computationally efficient PM power loss mapping for brushless AC PM machines with surface-mounted PM rotor construction. *IEEE Trans. Ind. Electron*., 2015, 62(12): 7391-7401.

[21] D Ede, K Atallah, W Jewell. Effect of axial segmentation of permanent magnets on rotor loss in modular permanent-magnet brushless machines. *IEEE Trans. Ind. Appl*., 2007, 43(5): 1207-1213.

[22] H Fang, D Li, R Qu, et al. Rotor design and eddy-current loss suppression for high-speed machines with a solid-PM rotor. *IEEE Trans. Ind. Appl*., 2018, 55(1): 448-457.

[23] M Zhou, X Zhang, W Zhao, et al. Influence of magnet shape on the cogging torque of a surface-mounted permanent magnet motor. *Chinese Journal of Electrical Engineering*, 2019, 5(4): 40-50.

[24] S S Nair, V I Patel, J Wang. Post-demagnetization performance assessment for interior permanent magnet AC machines. *IEEE Trans. Magn*., 2016, 52(4): 8102810.

[25] K Yamazaki, Y Fukushima, M Sato. Loss analysis of permanent magnet motors with concentrated windings-variation of magnet eddy-current loss due to stator and rotor shapes. *IEEE Trans. Ind. Appl*., 2009, 45(4): 1334-1342.

[26] J Wang, K Atallah, R Chin, et al. Rotor eddy-current loss in permanent-magnet brushless AC machines. *IEEE Trans. Magn*., 2010, 46(7): 2701-2707.

[27] K Yamazaki, M Shina, Y Kanou, et al. Effect of eddy current loss reduction by segmentation of magnets in synchronous motors: Difference between interior and surface types. *IEEE Trans. Magn*., 2009, 45(10): 4756-4759.

[28] Y Yang, B Bilgin, M Kasprzak, et al. Thermal management of electric machines. *IET Electr. Power Appl*., 2015, 7(2): 104-116.

[29] V Madonna, P Giangrande, M Galea, et al. Thermal analysis of fault-tolerant electrical machines for aerospace actuators. *IET Electr. Power Appl*., 2019, 13(7): 843-852.

Junqiang Zheng received his B.S. degree in electrical engineering from Jiangsu University, Zhenjiang, China, in 2014, where he is currently working toward a Ph.D. degree in electrical engineering. His research interests include machine design and electromagnetic field computation.

Wenxiang Zhao (M'08-SM'14) received B.S. and M.S. degrees from Jiangsu University, Zhenjiang, China, in 1999 and 2003, respectively, and a Ph.D. degree from Southeast University, Nanjing, China, in 2010, all in electrical engineering. He has been with Jiangsu University since 2003, where he is currently a professor with the School of Electrical Information Engineering. From 2008 to 2009, he was a research assistant with the Department of Electrical and Electronic Engineering, The University of Hong Kong, Hong Kong, China. From 2013 to 2014, he was a visiting professor with the Department of Electronic and Electrical Engineering, University of Sheffield, Sheffield, UK. His current research interests include electric machine design, modeling, fault analysis, and intelligent control. He has authored and co-authored over 250 technical papers in these areas.

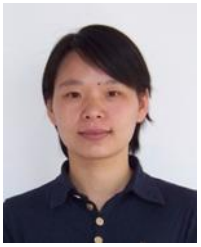

Jinghua Ji received B.S., M.S., and Ph.D. degrees in electrical engineering from Jiangsu University, Zhenjiang, China, in 2000, 2003, and 2009 respectively. Since 2000, she has been with the School of Electrical and Information Engineering, Jiangsu University, where she is currently a professor. From 2013 to 2014, she was a visiting scholar with the Department of Electronic and Electrical Engineering, University of Sheffield, Sheffield, UK. Her areas of interest include motor design and electromagnetic field computation. She has authored and co-authored over 100 technical papers in these areas.

Jihong Zhu received his B.S. degree in electrical engineering from Jiangsu University, Zhenjiang, China, in 1990, and a Ph.D. degree in control engineering from Nanjing University of Science and Technology, Nanjing, China, in 1995. From 1996 to 1997, he was with Nanjing University of Aeronautics and Astronautics, Nanjing, China, where he was a post doctor and an associate professor, respectively. Since 1998, he has been with Tsinghua University, where he is currently a professor. He has authored and co-authored over 150 technical papers, and is the holder of over 60 patents in the areas of his teaching and research interests, which include motor control and flight control.

Christopher H. T. Lee (M'12-SM'18) received his B.E. (First Class Honors) and Ph.D. degrees in electrical engineering from the Department of Electrical and Electronic Engineering, The University of Hong Kong, Hong Kong, China. He currently serves as an assistant professor in the School of Electrical and Electronic Engineering, Nanyang Technological University, Singapore, and is also a visiting scientist in the Research Laboratory of Electronics, Massachusetts Institute of Technology, USA. His research interests include electric machines and drives, renewable energies, and electric vehicle technologies. In these areas, he has published about 60 technical papers. Dr. Lee has received many awards, including the Li Ka Shing Prize (the best Ph.D. thesis award) and Croucher Foundation Fellowship.